





15 **Abstract:** Nanoplastic contamination is emerging as a significant threat to  
16 groundwater security on small islands, where freshwater lenses serve as primary  
17 water supplies. Existing groundwater management frameworks are largely based on  
18 salinity intrusion and do not account for the distinct transport behavior of nanoplastics.  
19 This study formulates a multi-physics numerical model incorporating variable-density  
20 groundwater flow, salt transport, and nanoplastic migration processes to investigate  
21 nanoplastic transport in idealized strip-island aquifers under pumping conditions. The  
22 model is calibrated using laboratory-scale data and evaluated at the field scale.  
23 Results show that nanoplastic migration is controlled not only by advection –  
24 dispersion processes but also by particle-specific interactions, leading to transport  
25 dynamics fundamentally different from those of dissolved salts. In particular, the  
26 higher effective dispersivity of nanoplastics causes earlier breakthrough at extraction  
27 wells and the formation of broader contaminant transition zones. Pronounced scale  
28 effects are observed: while laboratory simulations exhibit rapid upward coning and  
29 contamination, field-scale simulations indicate attenuated coning and stabilization  
30 over substantially longer timeframes. Sensitivity analysis identifies nanoplastic  
31 dispersivity as the dominant parameter influencing well contamination risk. These  
32 findings demonstrate that safe extraction strategies based solely on salinity thresholds  
33 may underestimate contamination risks and that well placement and pumping design  
34 must account for nanoplastic transition zones. The study provides a process-based  
35 framework for adapting groundwater management to emerging nanoplastic pollution  
36 in vulnerable island environments.



37 **Keywords:** Groundwater lens; Seawater intrusion; Groundwater contamination;

38 Pumping optimization

39



## 40 **1. Introduction**

41 Islands, more than 340,000 worldwide, cover approximately 6.7% of the Earth's  
42 terrestrial surface and support nearly 10% of the global population (Sayre et al., 2019).  
43 On many small islands, limited surface water availability makes groundwater a  
44 critical resource for local communities (Dose et al., 2014). Notably, numerous Pacific  
45 islands rely on shallow freshwater lenses—buoyant bodies of freshwater overlying  
46 saltwater in highly permeable aquifers—as their primary water supply (Sharan et al.,  
47 2021; White and Falkland, 2010). The formation, stability, and morphology of these  
48 lenses result from the interplay between density contrasts and multiple external  
49 factors, including climate, geological structures, and anthropogenic activities such as  
50 groundwater pumping and subsurface barrier installation (Alsumaiei and Bailey, 2018;  
51 Ketabchi et al., 2014; Tang et al., 2021, 2022; Yan et al., 2021; Yang et al., 2025; Gao  
52 et al., 2025; Zheng et al., 2025). A persistent challenge is the sustainable extraction of  
53 freshwater, as excessive pumping can induce upward saline coning, degrade water  
54 quality, and threaten long-term water security (Abdoulhalik and Ahmed, 2018; Dagan  
55 and Bear, 1968; Houben and Post, 2017; Werner et al., 2009).

56 The maximum safe extraction rate for freshwater lenses is typically estimated  
57 using analytical solutions that assume a sharp interface between freshwater and  
58 seawater (Muskat, 1937). Such approaches are widely used in two-dimensional  
59 strip-island models to determine the pumping threshold at which the saline interface  
60 reaches the well screen (Tang et al., 2020, 2021, 2024). While computationally  
61 efficient, these models neglect hydrodynamic dispersion and the development of a  
62 brackish transition zone, which can be extensive in highly permeable island aquifers  
63 (Coulon et al., 2022; Babu et al., 2020). Consequently, current safe-yield assessments  
64 often overlook realistic mixing processes and contaminant transport within the  
65 transition zone, potentially underestimating water-quality risks.

66 Beyond salinity intrusion, microplastic contamination has emerged as an  
67 additional and largely unaddressed threat to island groundwater systems.  
68 Microplastics are pervasive environmental pollutants detected in marine environments,



69 soils, and groundwater worldwide (Koelmans et al., 2022; Koutnik et al., 2021; Li et  
70 al., 2018; Ren et al., 2021; Thompson et al., 2024). Oceanic concentrations continue  
71 to rise due to plastic persistence and ongoing inputs (Isobe et al., 2019). The  
72 concentrations of nanoplastics—which are formed as a result of their breakdown—are  
73 even higher, with coastal waters often exhibiting higher levels than open-ocean  
74 regions (ten Hietbrink et al., 2025). Emerging evidence indicates that seawater  
75 intrusion facilitates the transport of microplastics into coastal aquifer systems (Chen  
76 et al., 2024). Because island aquifers are completely surrounded by seawater,  
77 freshwater lenses are particularly vulnerable to marine-sourced nanoplastic  
78 contamination (Fig. 1).

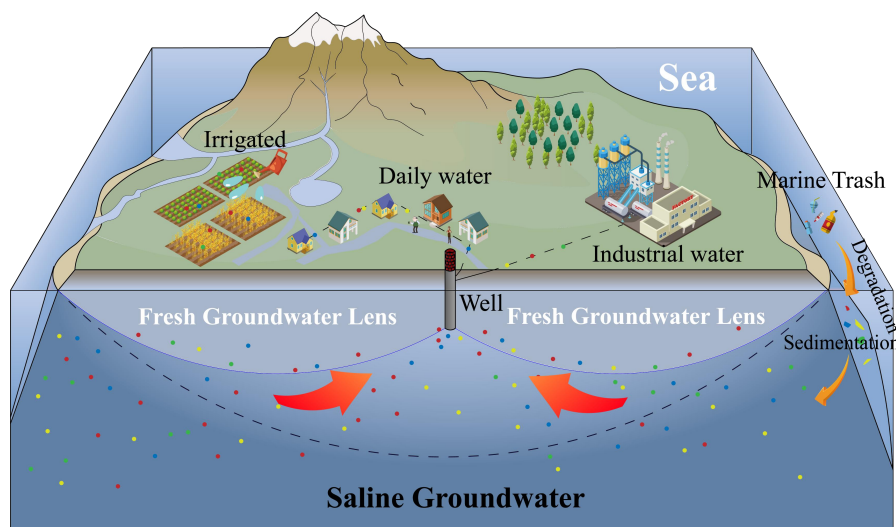
79 Transport processes of microplastics in porous media differ fundamentally from  
80 those of dissolved solutes. Early modeling efforts adapted classical  
81 advection-dispersion equations with simple adsorption terms (Babakhani et al., 2017),  
82 but subsequent studies have demonstrated that the migration of microplastics and  
83 nanoplastics involves additional mechanisms such as adsorption-desorption, clogging,  
84 interception, and aggregation (Liu et al., 2024; Yuan et al., 2024). Importantly,  
85 microplastic dispersion coefficients depend on particle size and flow velocity (Wang  
86 and Sedighi, 2023). Under pumping conditions that induce upward coning flow fields,  
87 these properties suggest that nanoplastics may migrate toward extraction wells more  
88 rapidly than salinity and form a broader or earlier contaminant transition zone.  
89 Traditional sharp-interface and salinity-based intrusion models fail to capture this  
90 behavior, which has remained largely unexplored in island freshwater lens studies.

91 Taken together, there are two critical gaps. First, existing safe-yield models  
92 oversimplify the freshwater-seawater transition zone by neglecting dispersion-driven  
93 mixing. Second, the distinct migration behavior of nanoplastics under  
94 pumping-induced coning remains poorly understood. Current modeling frameworks,  
95 largely derived from solute transport theory, do not adequately capture transient  
96 nanoplastic breakthrough or particle-specific transport dynamics.

97 To address these gaps, this study develops a coupled numerical model that



98 integrates variable-density groundwater flow, salt transport, and nanoplastic migration  
99 in island aquifers. This study aims to: (1) quantify marine-derived nanoplastic  
100 accumulation in freshwater extraction wells under pumping conditions; (2) assess how  
101 nanoplastic transport, especially enhanced dispersivity, alters the maximum safe  
102 extraction rate compared to traditional salinity-based thresholds; and (3) evaluate the  
103 sensitivity of nanoplastic migration and associated risks to key hydrogeological  
104 parameters and operational factors. By incorporating nanoplastic transport parameters  
105 derived from laboratory column experiments and conducting simulations at both  
106 laboratory and field scales, this work provides critical insights for adjusting  
107 groundwater management strategies to safeguard island freshwater resources in the  
108 face of emerging nanoplastic pollution.



109

110 Fig. 1. Schematic diagram of freshwater lenses and nanoplastic contaminant  
111 distribution in an idealized strip-island aquifer under groundwater extraction.

## 112 2. Methods

### 113 2.1 Mathematical model

114 To simplify the problem and enhance computational tractability, the following  
115 key assumptions are adopted based on established modeling practices in coastal  
116 aquifer studies (Stoeckl and Houben, 2012; Yao et al., 2019): (i) the aquifer is



117 homogeneous and isotropic; (ii) fluid density is solely dependent on groundwater  
118 salinity, with thermal effects considered negligible; (iii) the nanoplastic particle  
119 density is assumed to be approximately equal to the water density (e.g., some aged  
120 nanoplastics); (iv) the saturated zone is initially saturated with seawater, and rainfall  
121 infiltration is spatially uniform and temporally constant; and (v) groundwater flow is  
122 simulated within a two-dimensional vertical profile of the strip island, leveraging the  
123 geometric symmetry of the idealized domain.

124 This study presents an integrated numerical framework that extends a  
125 variable-density groundwater flow model for the unsaturated-saturated zone by  
126 incorporating salinity and nanoparticle transport modules. The nanoparticle transport  
127 model uniquely combines advective-diffusive transport with nanoplastic adsorption  
128 mechanisms. The resulting framework simultaneously simulates variable-density  
129 groundwater flow, solute salt transport, and nanoparticle migration via coupled  
130 advection-dispersion and adsorption processes. Governing equations for the  
131 variable-density flow and salinity transport components are available in Text S1.

132 Research suggests that nanoplastic transport is primarily influenced by particle  
133 movement and physical/physicochemical interactions with porous media surfaces (Al  
134 Harraq and Bharti, 2022; Ranjan et al., 2023; Ren et al., 2022; Waldschläger and  
135 Schüttrumpf, 2020). Particle movement is described in the equations as convection,  
136 diffusion and dispersion effects, while physicochemical interactions with porous  
137 media are characterized by mechanisms such as adhesion and detachment, mechanical  
138 strain on aggregates and individual particles, blockage, and maturation. The  
139 subsurface transport of nanoplastic particles is governed by an advection-diffusion  
140 equation, a framework established for nanoparticle migration that captures advection,  
141 dispersion, and adsorption processes (Yuan et al., 2024):

$$\frac{\partial}{\partial t}(S_w \theta C_{np}) + \frac{\partial}{\partial t}(\rho_b s) + \nabla C_{np} \frac{k_r \mathbf{k}}{\mu} \nabla P + \nabla \cdot [-\theta S_w D_{np} \nabla C_{np}] = f \quad (1)$$



$$\frac{\rho_b \partial s}{\partial t} = \theta K_{\text{att}} \psi_b C_{\text{np}} e^{-\frac{s}{\lambda}} - \rho_b K_{\text{det}} s + \theta \rho_b K_{\text{rip}} s C_{\text{np}} \quad (2)$$

142 where  $C_{\text{np}}$  represents the concentration of nanoplastics in groundwater [ $\text{ML}^{-3}$ ],  $\rho_b$   
143 denotes the density of the aquifer medium [ $\text{ML}^{-3}$ ],  $s$  is the mass of nanoplastics  
144 attached per unit mass of solid [ $\text{MM}^{-1}$ ],  $D_{\text{np}}$  is the hydrodynamic dispersion  
145 coefficient of nanoplastics [ $\text{L}^2\text{T}^{-1}$ ], and  $f$  is the source-sink term [ $\text{ML}^{-3}\text{T}^{-1}$ ].  $K_{\text{att}}$  is  
146 the first-order colloidal attachment coefficient [ $\text{T}^{-1}$ ], parameter  $\lambda$  represents the strain  
147 capacity of porous media [ $\text{MM}^{-1}$ ],  $K_{\text{det}}$  is the first-order colloidal detachment  
148 coefficient [ $\text{T}^{-1}$ ], and  $K_{\text{rip}}$  is the aging kinetic coefficient [ $\text{M}^{-1}\text{L}^3\text{T}^{-1}$ ].

149 The adhesion of nanoplastics in porous media is described by the following  
150 governing equation:

$$\psi_b = \left(1 - \frac{s}{s_{\text{max}}}\right) \quad (3)$$

151 where  $\psi_b$  denotes the adhesion state of nanoplastics in porous media [-], and  $s_{\text{max}}$   
152 represents the maximum mass of nanoplastics that can be retained per unit mass of  
153 porous medium [ $\text{MM}^{-1}$ ].

154 The variation in hydraulic conductivity as a function of porosity is characterized  
155 by the following relationship (Zheng, 2014):

$$\frac{K}{K_0} = \left(\frac{\theta}{\theta_0}\right)^3 \left(\frac{1-\theta_0}{1-\theta}\right)^3 \quad (4)$$

156 where  $K$  is the hydraulic conductivity of the porous medium [ $\text{LT}^{-1}$ ],  $K_0$  is the  
157 hydraulic conductivity of the initial porous medium [ $\text{LT}^{-1}$ ], and  $\theta_0$  is the porosity of  
158 the initial water-bearing medium [-].

159 The approximate analytical solution derived by Tang et al. (2021) describes the

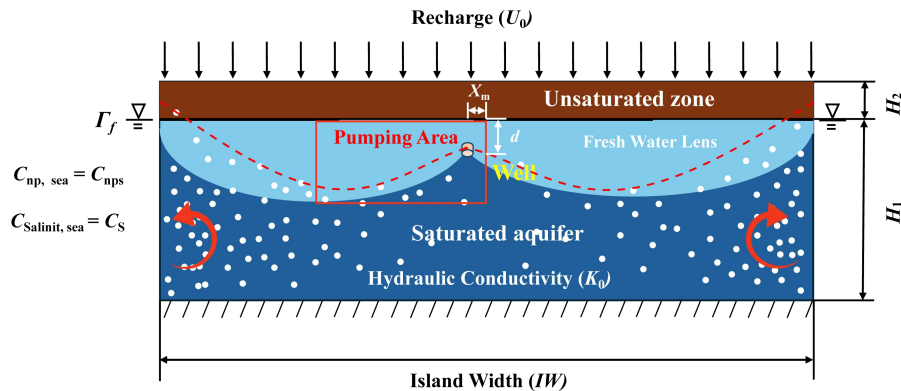


160 critical pumping rate preventing brine intrusion when pumping wells are located in  
 161 the idealized strip island's central region. The theoretical maximum safe extraction  
 162 rate is expressed as:

$$Q_{Tmax} = \omega(W - x_m) - \frac{\delta(1 + \delta)Kd^2}{(W - x_m)} \quad (5)$$

$$\delta = \frac{(\rho_s - \rho_f)}{\rho_f} \quad (6)$$

163 where  $\omega$  is the infiltration rate at the upper surface of the unsaturated zone [LT<sup>-1</sup>],  
 164  $\rho_s$  is the sea water density [ML<sup>-3</sup>],  $\rho_f$  is the fresh water density [ML<sup>-3</sup>],  $d$  is the  
 165 distance from the well to the lower boundary of the unsaturated zone [L],  $W$  is the half  
 166 width of the idealized strip island[L],  $x_m$  is the distance from the well to the centre  
 167 of the idealized strip island[L].



169 Fig. 2. Conceptual model of nanoplastic pollution in an idealized strip-island aquifer  
 170 with central pumping. The model depicts an unsaturated zone (height  $H_2$ ) over a  
 171 saturated zone (height  $H_1$ ). Freshwater lenses are shown in light blue and saline  
 172 groundwater in dark blue. Key parameters include island width ( $IW$ ), continuous  
 173 precipitation ( $U_0$ ), seawater salinity ( $C_s$ ), and seawater nanoplastic concentration  
 174 ( $C_{nps}$ ).



175 **2.2 Numerical Simulation**

176 The numerical simulation investigates the migration behavior of nanoplastics  
 177 under pumping conditions in an idealized strip-island aquifer. The laboratory-scale  
 178 model domain (60 cm×17 cm) was constructed following the configuration  
 179 established by Tang et al. (2021) (Fig. S4), while a field-scale model (600 m×50 m)  
 180 was developed to assess site-level transport phenomena. Key simulation parameters  
 181 are provided in Table 1. Model parameters calibrated from laboratory-scale  
 182 experiments were extrapolated to the field scale assumed for the modeling study to  
 183 evaluate the consistency of nanoplastic migration patterns across scales. At the ocean  
 184 boundary, a constant head (Dirichlet) condition was imposed with a specified  
 185 hydraulic head ( $H_1$ ) and a salt concentration of 34.7 g/L; tidal influences were  
 186 neglected. A constant flux (Neumann) condition was applied to the upper boundary,  
 187 representing recharge at a rate  $U_0$ . Fig. 2 shows a vertical cross-section of a typical  
 188 freshwater groundwater lens in an idealized island under single-well pumping  
 189 conditions. Additional aquifer properties are summarized in Table 1.

190 **Table 1.** Numerical Simulation Parameters for Variable-Density Flow and Nanoplastic  
 191 Transport (Laboratory and Field Scales)

Parameter	Sympol	Unit	Value
<i>Variable density parameter</i>			
Density of sea water	$\rho_0$	kg/m <sup>3</sup>	1025
Density of freshwater	$\rho_f$	kg/m <sup>3</sup>	1000
brine concentration	$C_s$	mol/L	0.5989
<i>Nanoplastics properties PS-Pd-1</i>			
Constant a, b	$\lambda$	mg/g	1.6
Particle deposition rate coefficient a, b	$K_{att}$	1/s	0.0025
Euler number a	e	—	2.7183
The maximum solid phase particle con centration a, b	$S_{max}$	m <sup>3</sup> /kg	10



Particle release rate coefficient a, b	$K_{det}$	1/s	0.001
Maturity rate of nanoplastics a, b	$K_{rip}$	$m^3/(s \cdot mol)$	0.009
Longitudinal dispersivity b	$\alpha_{LPS-Pd-1}$	cm	1.06
The average relative molecular weight of nanoplastics c	$N_m$	g/mol	70000
<b><i>Nanoplastics properties PS-Pd-2</i></b>			
Constant a, b	$\lambda$	mg/g	1.7
Particle deposition rate coefficient a, b	$K_{att}$	1/s	0.0002
The maximum solid phase particle concentration a, b	$S_{max}$	$m^3/kg$	10
Particle release rate coefficient a, b	$K_{det}$	1/s	0.005
Maturity rate of nanoplastics a, b	$K_{rip}$	$m^3/(s \cdot mol)$	0.007
Longitudinal dispersivity b	$\alpha_{LPS-Pd-2}$	cm	0.91
The average relative molecular weight of nanoplastics c	$N_m$	g/mol	70000
<b><i>Laboratory Porous medium properties</i></b>			
Island width d	$IW$	cm	60
Saturated zone thickness d	$H_1$	cm	15
Unsaturated zone thickness d	$H_2$	cm	2
Rainfall infiltration d	$U_0$	cm/min	0.80
Porosity d	$\theta_0$	—	0.38
Longitudinal dispersivity	$\alpha_L$	cm	0.2
Hydraulic conductivity d	$K_0$	cm/min	200
<b><i>Field-scale Porous medium properties</i></b>			
Island width	$IW$	m	600
Saturated zone thickness	$H_1$	m	45
Unsaturated zone thickness	$H_2$	m	5
Rainfall infiltration	$U_0$	m/s	$2 \times 10^{-8}$



Porosity	$\theta_0$	—	0.38
Longitudinal dispersivity	$\alpha_L$	m	0.5
Hydraulic conductivity	$K_0$	m/s	0.0001

192 a. Data from Liu et al. (2024)

193 b. Data inversion was performed based on the experimental.

194 c. Data from Singh et al. (2025)

195 d. Experimental water pumping scenario from Tang et al. (2021)

196 The coupled governing equations for variable-density saturated groundwater  
 197 flow and solute transport were solved numerically via COMSOL Multiphysics, with  
 198 boundary conditions prescribed accordingly. The system of equations was solved  
 199 iteratively using a preconditioned conjugate gradient (PCG) method with a relative  
 200 tolerance of  $1 \times 10^{-4}$ . Initial time steps of 0.001 s and 0.001 d were adopted for the  
 201 transient analyses.

202 The computational domain for the laboratory-scale model was discretized into  
 203 63,928 triangular elements and 32,350 nodes, with a maximum element diameter of 2  
 204 mm. For the field-scale model, the domain was discretized into 30,000 quadrilateral  
 205 elements and 30,651 nodes, with a maximum element diameter of 1 m. The selected  
 206 mesh sizes, in conjunction with the hydrodynamic dispersion parameters, conformed  
 207 to the Péclet number criterion to minimize numerical dispersion and ensure solution  
 208 stability (Voss and Provost, 2002):

$$Pe_1 = \frac{v_1 \Delta L_1}{D_1 + \alpha_{L1} v_1} \approx \frac{\Delta L_1}{\alpha_{L1}} = 1 \leq 4 \quad (7)$$

$$Pe_2 = \frac{v_2 \Delta L_2}{D_2 + \alpha_{L2} v_2} \approx \frac{\Delta L_2}{\alpha_{L2}} = 2 \leq 4 \quad (8)$$

209 where  $Pe_1$  is the Péclet number in laboratory-scale [-],  $Pe_2$  is the Péclet number in  
 210 site-scale [-],  $\Delta L_1$  is the grid length in laboratory-scale [L],  $\Delta L_2$  is the grid length  
 211 in site-scale [L],  $v_1$  is flow velocity in laboratory-scale [ $LT^{-1}$ ],  $v_2$  is flow velocity in



212 site-scale [ $LT^{-1}$ ],  $D_1$  is diffusion coefficient in laboratory-scale [ $L^2T^{-1}$ ],  $D_2$  is  
213 diffusion coefficient in site-scale [ $L^2T^{-1}$ ],  $\alpha_{L1}$  is the Longitudinal dispersivity in  
214 laboratory-scale [L],  $\alpha_{L2}$  is the Longitudinal dispersivity in site-scale [L].

215 A continuous rainfall-driven model was developed to simulate freshwater lens  
216 dynamics and well extraction in an idealized island aquifer. The simulation comprises  
217 two distinct hydraulic phases: Phase I involves the formation of a stable freshwater  
218 lens under continuous rainfall infiltration and seawater intrusion; Phase II initiates  
219 groundwater extraction via a single pumping well, leading to the development of a  
220 stable saline upconing zone. In the laboratory-scale setup, the horizontal distance  $x_m$   
221 from the standard well to the island center was set to 0, 2.5, 5, 7.5, 10, 12.5, 15, 17.5,  
222 and 20 cm. The vertical distance  $d$  from the well screen to the base of the saturation  
223 zone was defined as 0, 5, 10, 12, 15, 18, 20, and 25 mm. Hydraulic conductivity  $K_0$   
224 values were assigned as 150, 175, 200, 225, and 250 cm/min, with corresponding  
225 recharge rates  $U_0$  of 0.6, 0.7, 0.8, 0.9, and 1.0 cm/min. For the field-scale scenario, the  
226 pumping well was positioned at a horizontal distance  $x_m=5$  m from the island center,  
227 corresponding to a central well location. The hydraulic conductivity  $K_0$  was set to  
228  $1 \times 10^{-4}$  m/s, with a recharge rate  $U_0 = 2 \times 10^{-8}$  m/s (Tang et al., 2021).

### 229 **2.3 Evaluation Indicators**

230 Nanoplastic concentrations at the wellhead were monitored to evaluate the  
231 impacts of nanoplastics on island freshwater lens development projects. The  
232 seawater-freshwater interface of the freshwater lens was designated as 0.347 g/L,  
233 corresponding to 1% seawater salinity. Contemporary laboratory investigations  
234 typically utilize nanoplastic concentrations ranging from 10  $\mu\text{g/L}$  to 100 mg/L. Owing  
235 to constraints associated with nanoplastic preparation protocols and detection  
236 capabilities, the migration parameters of nanoplastics in this study were derived under  
237 an initial concentration of 10 mg/L. To date, the highest measured nanoplastic  
238 concentrations in natural environments have reached 3.02 mg/L in the North Pacific,  
239 while a maximum concentration of 162 mg/L has been documented in relevant studies



240 (Moore et al., 2001; Reddy et al., 2006). Sussarellu et al. (2016) reported that a  
241 nanoplastic concentration of 22  $\mu\text{g/L}$  induced alterations in feeding behavior and  
242 reproductive disruption in oysters. Adopting the 1% seawater salinity threshold as a  
243 reference for nanoplastic concentrations facilitates comparisons of migration patterns  
244 between nanoplastics and dissolved salts under freshwater extraction scenarios in  
245 idealized strip-shaped islands, while incorporating the biological toxicity of  
246 nanoplastics as a critical constraint.

247 Concurrently, the distribution of nanoplastics within freshwater lenses is  
248 characterized by comparing the volume reduction rate ( $VR$ ) of freshwater lenses over  
249 a given time period:

$$VR = \frac{V_0}{V_w} \quad (9)$$

250 where  $V_0$  represents the volume of freshwater lenses not yet pumped [ $\text{L}^3$ ],  $V_w$   
251 represents represents the volume of freshwater lenses after pumped [ $\text{L}^3$ ],

252 Accounting for the implications of the transition zone theory for groundwater  
253 pumping practices, the following indicator is defined: the ratio of the actual maximum  
254 safe extraction capacity to the theoretical maximum safe extraction capacity ( $ASYR$ ):

$$ASYR = \frac{Q_{Amax}}{Q_{Tmax}} \quad (10)$$

255 where  $Q_{Amax}$  represents the actual maximum safe extraction volume [ $\text{L}^3\text{T}^{-1}$ ],  $Q_{Tmax}$   
256 represents the theoretical maximum safe extraction volume [ $\text{L}^3\text{T}^{-1}$ ]

257 Taking into account the potential reduction in groundwater extraction capacity  
258 induced by nanoplastic contamination, the following indicator is defined: the ratio of  
259 the maximum safe extraction capacity reduction caused by nanoplastic retention to the  
260 maximum safe extraction capacity ( $RRSY$ ):



$$RRSY = \frac{Q_{Amax} - Q_{Smax}}{Q_{Amax}} \quad (11)$$

261 where  $Q_{Smax}$  represents the maximum safe extraction volume without nanoplastic  
262 influence [ $L^3T^{-1}$ ].

#### 263 **2.4 Model Calibration**

264 This study examined the migration patterns of two synthetic nanoplastics  
265 (PS-Pd-1 and PS-Pd-2) that exhibit contrasting hydrophobicity. The detailed synthesis  
266 protocols are available in Supplementary Materials (Text S2). To ensure model  
267 accuracy, migration parameters for nanoplastics in quartz sand (Table 1) were  
268 validated using column experiment data from Liu et al. (2024). The experimental  
269 setup and methodology are detailed in Text S3 and Fig. S1, with calibration processes  
270 and results illustrated in Fig. S2 and S3. The primary objective was to quantify how  
271 differential nanoplastic-solid phase interactions influence contamination levels in  
272 freshwater lenses (Amirmoshiri et al., 2020; Wang et al., 2021). As summarized in  
273 Table 1, PS-Pd-1 exhibits strong solid-phase adsorption capacity, whereas PS-Pd-2  
274 demonstrates weaker adsorption. Given potential scale-dependence in nanoplastic  
275 transport parameters, current research remains largely focused on laboratory-scale  
276 investigations (Johnson, 2020; Li et al., 2021; Liu et al., 2024).

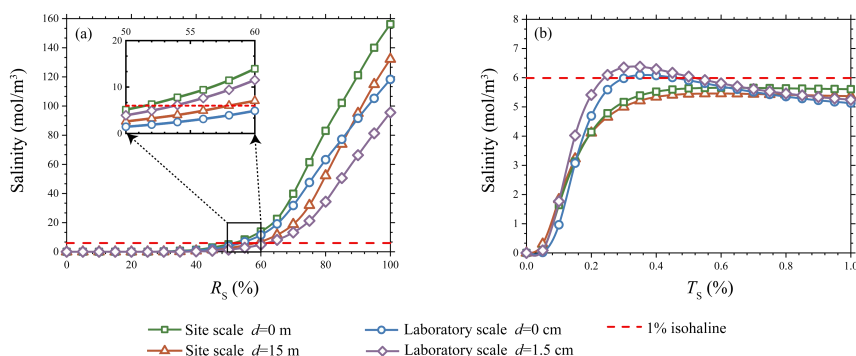
277 A single-well extraction scheme was implemented in the central region of an  
278 idealized strip island aquifer. The maximum safe extraction rate, calculated based on  
279 sharp-interface theory, served as the baseline scenario. However, the applicability of  
280 this theoretical maximum for island freshwater lenses requires critical re-evaluation,  
281 as previous sharp-interface analytical and numerical studies have largely neglected the  
282 transition zone formed by salinity dispersion and diffusion—a factor addressed in  
283 only limited corrections (Coulon et al., 2022). To determine a more accurate  
284 maximum safe extraction rate, a series of numerical simulations with predefined  
285 pumping rates were conducted to calibrate both laboratory-scale and site-scale  
286 conceptual models.

287 Although Tang et al. (2021) provided preliminary numerical validation via Fig.



288 S4(a)(b), their simulations omitted the effects of the unsaturated zone and the salinity  
 289 transition zone. In contrast, our validation-based simulations (Fig. S4(c)(d)), which  
 290 incorporate the unsaturated zone and employ dispersion parameters consistent with  
 291 Chen et al. (2024), indicate that the 1% salinity contour exceeds the well bottom  
 292 elevation by 2.03 m. This signifies that pumping-induced salinity surpasses regulatory  
 293 thresholds, necessitating a reduction in extraction volume.

294 The relationship between well salinity and the extraction volume ratio (actual to  
 295 theoretical) is illustrated in Fig. 3. Results confirm that the presence of the unsaturated  
 296 and transition zones reduces the extraction capacity to 50%–60% of the theoretical  
 297 maximum ( $Q_{Tmax}$ ). Specifically, under laboratory conditions, the maximum safe  
 298 extraction capacity decreased to 61% and 53% of  $Q_{Tmax}$  for shallow ( $d=0$  cm) and  
 299 deep ( $d=1.5$  cm) extraction scenarios, respectively (Fig. 3(a)). Corresponding  
 300 field-scale simulations showed reductions to 57% and 51% of  $Q_{Tmax}$  for shallow ( $d=0$   
 301 m) and deep ( $d=15$  m) extraction. The temporal evolution of well salinity during  
 302 freshwater lens re-stabilization (Fig. 3(b)) further demonstrates that salinity  
 303 stabilization occurs within 12 minutes at the laboratory scale but requires  
 304 approximately 4.5 years at the field scale, highlighting significant temporal disparities  
 305 influenced by scale effects.



306

307 Fig. 3. Variations in well salinity as a function of the ratio of extraction volume to  
 308 theoretical maximum ( $R_s$ ) and the ratio of time to theoretical equilibrium time ( $T_s$ )  
 309 during pumping at different depths, measured at both field and laboratory scales: (a)



310 Well salinity versus extraction volume, with the magnified region indicating the  
311 extraction volume range where well concentration approaches the 1% isohaline; (b)  
312 Temporal concentration variations for wells with salinity near the 1% isohaline in  
313 panel (a).

### 314 **3. Results and Discussion**

#### 315 **3.1 Distribution Patterns of Nanoplastics Under Pumping Conditions**

316 Hydrophobic microplastics (NPs) were selected as the primary research focus of  
317 this study. Text S4 and Fig. S5 demonstrate that hydrophobic molecules exhibit higher  
318 mobility and pose more significant hazards than hydrophilic counterparts under  
319 simulated single-well pumping conditions.

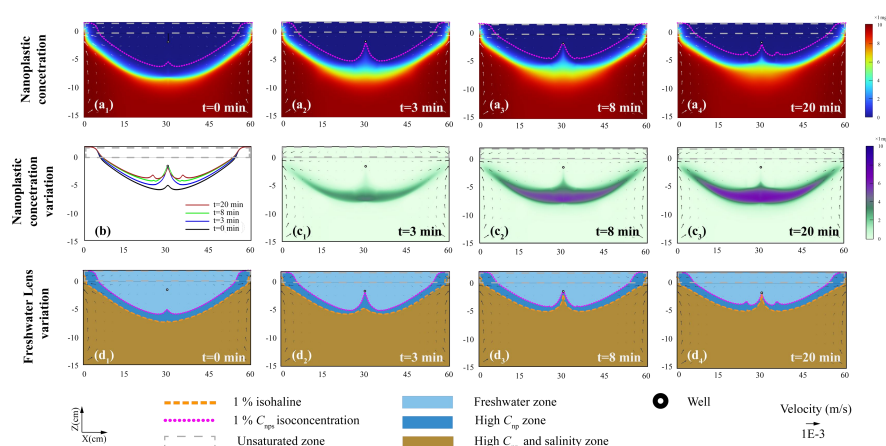
320 Fig. 4(a<sub>1</sub>-a<sub>4</sub>) illustrates an “upper cone” phenomenon in nanoplastic  
321 concentrations during pumping, analogous to that of salinity. Fig. 4(a<sub>1</sub>) reveals that  
322 highly dispersive nanoplastics may form anomalous distributions in the central  
323 banded region of the island—a zone previously referred to as the “stagnation zone”  
324 (Wang et al., 2023). Nearshore aquifers on both sides of the island undergo intense  
325 convection, driven by groundwater discharge to the sea and seawater intrusion  
326 induced by density currents. At the laboratory scale, this convective zone spans  
327 approximately 10 cm; at the field scale, it extends to around 100 meters, where  
328 groundwater Darcy velocities exceed  $1 \times 10^{-3}$  m/s. In contrast, velocities within the  
329 central “stagnation zone” remain below  $1 \times 10^{-8}$  m/s. This zone is dominated by weak  
330 convection, with material transport in groundwater primarily governed by dispersion  
331 and interactions with the solid phase.

332 Fig. 4(b) presents dynamic nanoplastic isoconcentration lines at the wellhead,  
333 where concentrations first increase and then decrease—indicating that wellhead  
334 nanoplastics are influenced by the “stagnation zone”. The discrepancy in migration  
335 behavior between nanoplastics and dissolved solutes stems primarily from their  
336 distinct physicochemical properties: as colloidal particles, nanoplastic migration is  
337 regulated not only by advection-dispersion but also by particle-medium interactions



338 (e.g., adsorption-desorption, clogging, and filtration). Fig. 4(c<sub>1</sub>-c<sub>3</sub>) depicts variations  
 339 in nanoplastic concentrations. Nanoplastics extracted from the well resulted in an  
 340 additional 37.48% reduction in the initial freshwater lens area, while the maximum  
 341 depth of freshwater bodies surrounded by nanoplastics increased by 0.030 m.

342 Fig. 4(d<sub>1</sub>-d<sub>4</sub>) compares the distribution patterns of salinity and nanoplastics,  
 343 revealing that nanoplastics exceeding 1% of the critical nanoplastic concentration  
 344 ( $C_{nps}$ ) are concentrated within freshwater lens layers. With the disappearance of the  
 345 original “stagnation zone”, a new flow field transition zone is formed, triggering the  
 346 emergence of a new “stagnation zone”. The proportion of the freshwater lens  
 347 occupied by the nanoplastic transition zone (dark blue areas in Fig. 4(d<sub>1</sub>-d<sub>4</sub>)) increased  
 348 from 30.27% to 41.24%. Compared to dissolved solutes, nanoplastics possess larger  
 349 hydrodynamic diameters and unique surface properties, leading to distinctive  
 350 migration patterns in porous media.



351

352 Fig. 4. Distribution and concentration dynamics of PS-Pd-2 hydrophobic nanoplastics  
 353 and corresponding freshwater lens alterations at the laboratory scale (60 cm×17 cm)  
 354 during pumping ( $R_S = 53\%$ ): (a<sub>1</sub>-a<sub>4</sub>) freshwater lenses demarcated by the 1%  
 355 isoconcentration line of PS-Pd-2 hydrophobic nanoplastics at 0, 3, 8 and 20 minutes  
 356 post-pumping, (b) temporal variation of the 1%  $C_{nps}$  isoconcentration line, (c<sub>1</sub>-c<sub>3</sub>) net  
 357 concentration variations relative to the baseline (0 min) at 3, 8 and 20 minutes



358 post-pumping, ( $d_1$ - $d_4$ ) spatial offset between the 1% isohaline and 1%  $C_{nps}$   
359 isoconcentration line around the freshwater lens.

360 Fig. 5(a) presents the vertical concentration profile of nanoplastics at the  
361 wellhead, further validating the aforementioned mechanism. Prior to pumping  
362 initiation, the nanoplastic transition zone was situated 0.07 - 0.10 m below the well  
363 bottom. Following pumping initiation, the transition zone underwent a rapid upward  
364 migration and expansion to 0.02 m below the well bottom. Thirty minutes  
365 post-pumping, although the transition zone exhibited a slight recession, a stable  
366 transition zone was maintained at 0.06 m below the well bottom, while a new steep  
367 transition zone formed at 0.03 m. nanoplastic concentrations at the wellhead increased  
368 markedly within the first 4 minutes, started to decline after 8 minutes, stabilized at 30  
369 minutes post-pumping, and ultimately converged with the concentration trends of  
370 chloride ( $Cl^-$ ), indicating that solute and colloidal transport are governed primarily by  
371 convection. The observed transport behavior can be interpreted through the lens of  
372 effective dispersion parameters. In porous media transport modeling, the macroscopic  
373 dispersion coefficient in advection-dispersion equations serves as an effective  
374 parameter that implicitly captures the integrated effects of various pore-scale  
375 processes, including particle-pore interactions, flow path tortuosity, and temporary  
376 retention at pore throats. While these microscopic processes are not explicitly  
377 resolved in the current continuum-scale model, their integrated effects are reflected in  
378 the calibrated dispersion parameters.

379 Fig. 5(b) illustrates the dynamic concentration dynamics of hydrophilic and  
380 hydrophobic nanoplastics, both of which exhibit an initial increase followed by a  
381 subsequent decrease. During the initial pumping phase (0 - 6 min), high-concentration  
382 nanoplastics in the immediate vicinity of the well were the primary fraction extracted  
383 by pumping, leading to a sharp concentration increase to a peak of 2.489%  $C_{nps}$ . With  
384 prolonged pumping (6 - 32 min), relatively low-nanoplastic peripheral groundwater  
385 gradually infiltrated the pumping-affected zone. The original stagnation zone was  
386 reconfigured under the influence of pumping, with new stagnation zones emerging on

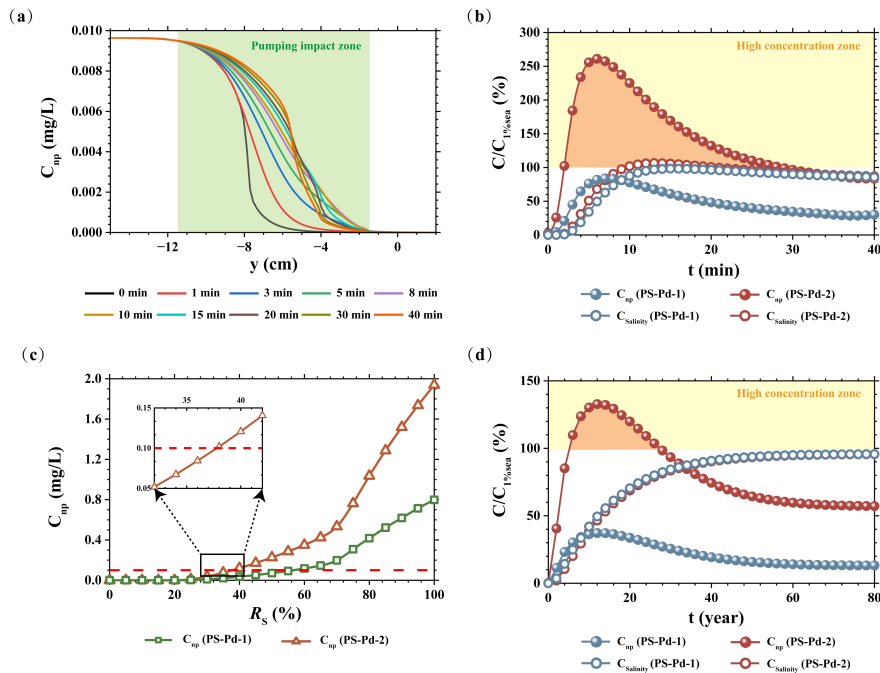


387 both sides of the well. The system eventually attained a state of dynamic equilibrium  
388 after 32 min of pumping, with nanoplastic concentrations stabilizing at a steady level.  
389 Notably, salinity variations under distinct contamination scenarios involving  
390 hydrophilic and hydrophobic nanoplastics also exerted a notable regulatory influence  
391 on this process. This phenomenon is hypothesized to originate from an approximate  
392 40% reduction in hydraulic conductivity, which is induced by the solid-phase  
393 enrichment of hydrophilic nanoplastics in specific central regions of the study  
394 domain.

395 With respect to the distinct distribution characteristics of wellborne hydrophobic  
396 nanoplastics presented in Fig. 5(b), which diverge from those of salinity, the  
397 application of a 1% concentration threshold to nanoplastics (consistent with the  
398 salinity threshold) results in wellhead nanoplastic concentrations exceeding this  
399 criterion for more than 80% of the duration prior to the attainment of a stable system  
400 state. To mitigate the adverse impacts of the extensive dispersion of hydrophobic  
401 nanoplastics on the quality of pumped groundwater, Fig. 5(c) presents the correlations  
402 between hydrophilic and hydrophobic nanoplastic concentrations at the wellhead and  
403 the cumulative pumped water volume. Under the theoretical maximum safe pumping  
404 rate, hydrophobic nanoplastics accumulate at the wellhead to a concentration of 1.939  
405 mg/L during the initial pumping phase. To reduce the initial wellhead nanoplastic  
406 concentrations to below the 1%  $C_{nps}$  threshold, the actual maximum safe pumping rate  
407 must be further reduced to 37% of the theoretical maximum safe pumping rate. Fig.  
408 5(d) verifies that this identical phenomenon is observable in wellhead nanoplastic  
409 concentrations at the field scale, where nanoplastics at such concentrations are still  
410 rapidly entrained into the pumping well—indicating that the enrichment mechanism  
411 driven by high nanoplastic dispersibility remains valid at the field scale.  
412 High-concentration nanoplastic influxes at the wellhead persisted over a 5 - 28 year  
413 timeframe at the field scale. Conversely, nanoplastic concentrations in the upper cone  
414 region are comparatively lower, with those in the island's pumping wells reaching  
415 only 1.329 %  $C_{nps}$ . A detailed elucidation of the underlying mechanisms for this



416 phenomenon is presented in Section 3.2.



417  
 418 Fig. 5. Concentration dynamics at laboratory and field scales and their responses to  
 419 pumping rate adjustments: (a) 1%  $C_{nps}$  isoconcentration line variation along the  
 420 central axis ( $x=30$  cm) at laboratory scale; (b) Temporal variations in salinity and  
 421 nanoplastic concentrations for hydrophilic and hydrophobic nanoplastics at laboratory  
 422 scale; (c) Well nanoplastic concentration as a function of pumped  
 423 volume-to-theoretical maximum ratio ( $R_s$ ) for groundwater nanoplastics of distinct  
 424 hydrophilic-hydrophobic properties; (d) Temporal variations in well salinity and  
 425 nanoplastic concentrations for hydrophilic and hydrophobic nanoplastics at field  
 426 scale.

### 427 3.2 Scale Effects on Nanoplastic Transport

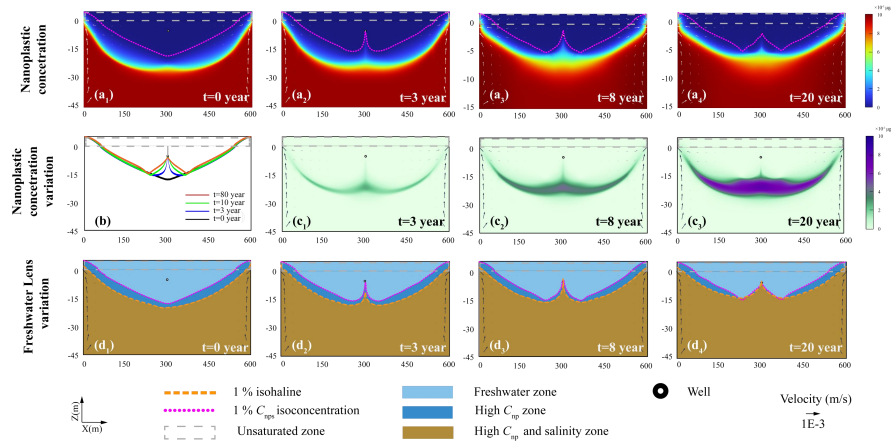
428 In field-scale simulations, the background concentration of hydrophobic  
 429 nanoplastics was set to  $1 \mu\text{g/L}$  ( $C_{nps}$ ). Dispersion parameters were adjusted based on  
 430 scaling-up experience (Gelhar et al., 1992), with the corresponding simulation results  
 431 presented in Fig. 6. Fig. 6(a<sub>1</sub>) shows that following stabilization of the freshwater lens,  
 432 the 90%–10%  $C_{nps}$  transition zone in the central island region thickened to more than



433 10 m, yet no prominent dispersion-driven upward cone formed in the island's core  
434 area. Scale effects exert their influence primarily in two aspects: with increasing scale,  
435 the heterogeneity of the aquifer medium becomes more complex, which may mask the  
436 unique migration behavior of nanoplastics. Additionally, streamline curvature is  
437 reduced and flow velocity distributions are more homogeneous at larger scales,  
438 thereby attenuating inertial effects.

439       Upon pumping initiation at the field scale, the depth of the freshwater lens  
440 decreased from 20.168 m to 13.785 m, while the maximum depth of the freshwater  
441 lens encircled by nanoplastics decreased from 17.943 m to 14.610 m. Fig. 6(c<sub>1</sub>-c<sub>3</sub>)  
442 depicts variations in nanoplastic concentration within the lens: the volumetric fraction  
443 of nanoplastics occupying the freshwater lens decreased from 31.48% to 23.40%, a  
444 trend that deviates from the increasing pattern observed at the laboratory scale. Fig.  
445 6(d<sub>1</sub>-d<sub>4</sub>) reveals the existence of a ~3 m-thick residual dissolved nanoplastic layer  
446 within the freshwater lens, with concentrations at 1-5% of the nanoplastic  
447 concentration in seawater. Upon stabilization of pumping, the transition zone migrated  
448 upward toward the bilateral jet zones but no new upward cone was generated. At the  
449 field scale, the enhancement of nanoplastic dispersion relative to solute dispersion  
450 was no longer pronounced, a phenomenon likely due to improved flow stability and  
451 inherent scale effects. In addition, the residence time of colloidal filtration and  
452 entrainment processes is extended at this scale, which may consequently modify the  
453 final spatial distribution of nanoplastics.

454



455

456 Fig. 6. Hydrophobic nanoplastic concentration dynamics and corresponding  
 457 freshwater lens alterations at field scale (600 m×50 m) during pumping ( $R_s = 51\%$ ):  
 458 (a<sub>1</sub>-a<sub>4</sub>) Freshwater lenses demarcated by the 1% PS-Pd-2 nanoplastic isoconcentration  
 459 line at 0, 3, 8 and 20 years post-pumping; (b) 1%  $C_{nps}$  isoconcentration line variation;  
 460 (c<sub>1</sub>-c<sub>3</sub>) Net nanoplastic concentration variations relative to the initial time point (0  
 461 year) at 3, 8 and 20 years post-pumping; (d<sub>1</sub>-d<sub>4</sub>) Spatial offset between the 1%  
 462 isohaline and 1%  $C_{nps}$  isoconcentration line around the freshwater lens.

### 463 3.3 Sensitivity Analysis

464 Four factors were selected for analysis, with the  $VR$ ,  $ASYR$ , and  $RRSY$  metrics  
 465 employed to evaluate nanoplastic contamination in freshwater and freshwater lenses,  
 466 as well as its implications for pumping operations.

467 Fig. 7(a<sub>1</sub>, b<sub>1</sub>) demonstrates that dispersion exhibits a significant correlation with  
 468  $VR$ , and nanoplastic dispersivity exerts a notable influence on pumping efficiency.  
 469 When nanoplastic dispersivity is lower than that of solutes, the distribution range of  
 470 nanoplastics closely approximates that of solutes, resulting in a narrow transition zone,  
 471 while  $Q_{Amax}$  is exclusively governed by salinity. When nanoplastic dispersivity equals  
 472 that of solutes, the freshwater lens zone formed by nanoplastics nearly perfectly  
 473 overlaps with the seawater-enclosed area. As dispersivity increases to 10 times that of  
 474 solutes, the volume of freshwater lenses decreases by approximately 30%. When the



475 dispersivity of residual nanoplastics exceeds 17 times that of salinity, the expanded  
476 dispersion range causes the 1%  $C_{nps}$  isoconcentration line to cover the wellhead area.  
477 The high sensitivity of nanoplastic behavior to dispersivity stems from their  
478 particulate nature: nanoplastics migrate not only via hydraulic dispersion but also  
479 through mechanisms such as Brownian motion, gravitational settling, and media  
480 interception. High dispersivity reflects the selective migration capacity of nanoplastics  
481 within complex pore structures, which is closely associated with their surface  
482 properties and hydrodynamic characteristics.

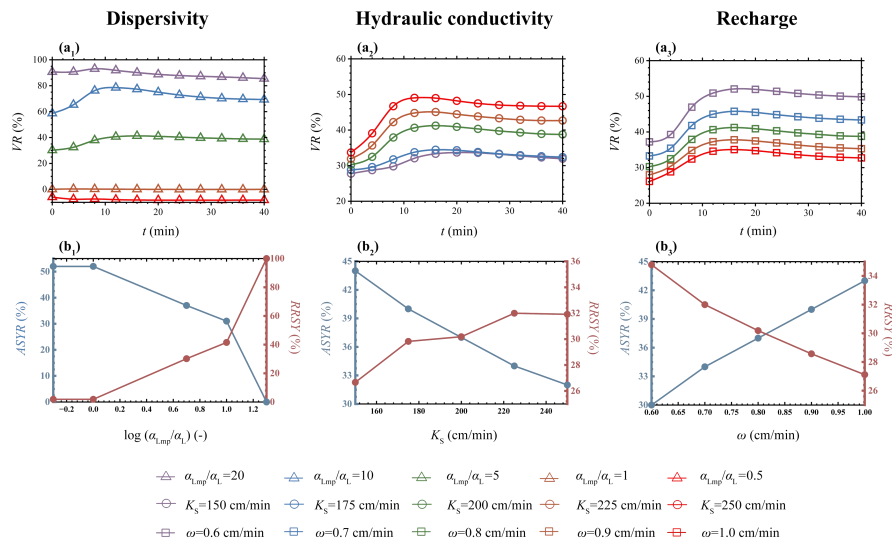
483 Fig. 7(a<sub>2</sub>,b<sub>2</sub>) reveals that  $VR$  gradually increases with rising hydraulic  
484 conductivity. At a hydraulic conductivity of 250 cm/min, 46.68% of the freshwater  
485 lens area is occupied by high-concentration nanoplastics. Under pumping conditions,  
486 both high hydraulic conductivity and high-permeability media result in a significant  
487 reduction in the usable portion of freshwater lens layers surrounded by nanoplastics.  
488 Aquifer hydraulic conductivity is another critical parameter regulating solute  
489 migration and retention. Previous studies have demonstrated that higher hydraulic  
490 conductivities result in reduced freshwater lens volumes and correspondingly  
491 decreased groundwater availability (Bailey and Jenson, 2014; Cui et al., 2021; Gao et  
492 al., 2025). The spatial distribution and magnitude of freshwater lenses surrounded by  
493 nanoplastics are consistent with these findings. High hydraulic conductivity  
494 accelerates freshwater discharge on both sides of the island, reducing the area where  
495 freshwater lenses can maintain equilibrium. For nanoplastics, increased hydraulic  
496 conductivity enhances flow velocity and convective transport capacity, thereby  
497 facilitating their intrusion into freshwater lenses.

498 Recharge rates were used to simulate precipitation intensity on the island. Fig.  
499 7(a<sub>3</sub>) shows that precipitation significantly reduces the spatial distribution density of  
500 nanoplastics within freshwater lenses, with this effect being pronounced both before  
501 and after pumping. Increased recharge leads to a decrease in  $VR$ ; when recharge rises  
502 to 1.0 cm/min,  $VR$  declines to 33%. Conversely, when recharge drops below 0.65  
503 cm/min, the final variation in  $VR$  also weakens, suggesting that nanoplastic



504 concentrations are more difficult to mitigate with increased pumping intensity. Fig.  
 505 7(b<sub>3</sub>) illustrates that enhanced recharge reduces the volume occupied by  
 506 high-concentration nanoplastics in freshwater lenses, significantly increasing  
 507 exploitable freshwater volume and alleviating the impact of nanoplastics on maximum  
 508 safe pumping rates. Previous studies indicate that the volume and thickness of island  
 509 freshwater lenses are positively correlated with precipitation (Zheng et al., 2025). The  
 510 "flushing effect" of precipitation on nanoplastic distribution likely operates through  
 511 two mechanisms: first, precipitation acts as the main source of freshwater storage in  
 512 lenses. As the freshwater lens area expands, the thick transition zone formed by  
 513 hydrophobic nanoplastics remains unaffected by convection and maintains a constant  
 514 thickness, leading to a reduced proportion of nanoplastics despite unchanged total  
 515 volume. Second, increased recharge may expand the strong convection zones on both  
 516 sides of the seawater boundary, shrinking the central "stagnation zone" and thereby  
 517 relatively weakening dispersion effects.

518 Among the analyzed media and environmental conditions, dispersivity emerges  
 519 as the key parameter governing nanoplastic retention behavior in freshwater lenses,  
 520 with high dispersivity exerting the most pronounced inhibitory effect on  $Q_{Amax}$ .



521

522 Fig. 7. The volume reduction rate of freshwater lenses (VR), the ratio of actual



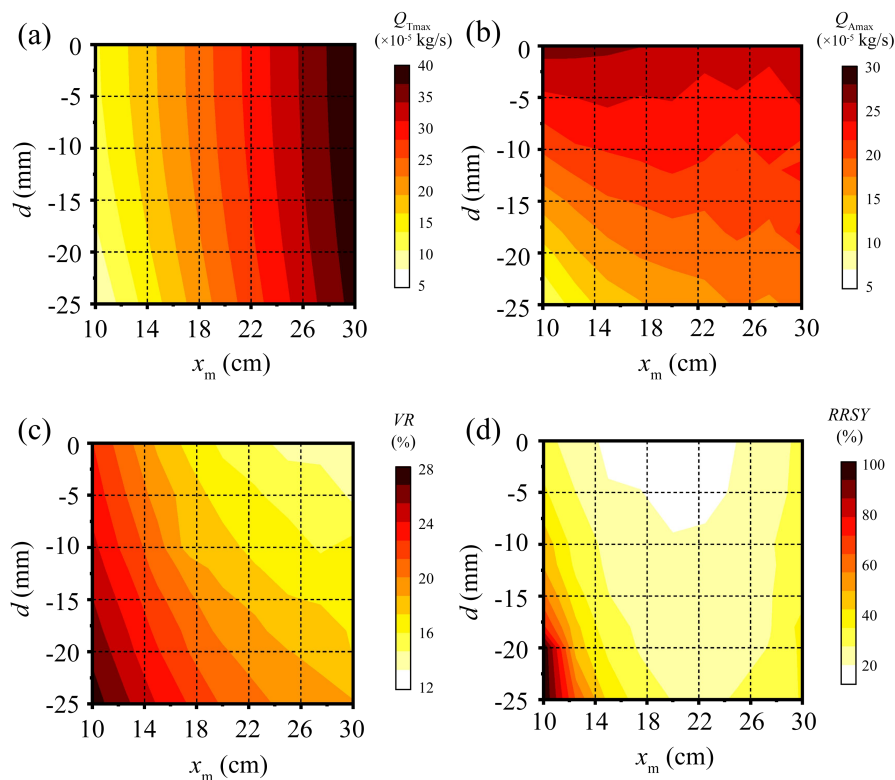
523 maximum safe extraction capacity to theoretical maximum safe extraction capacity  
524 ( $AS_{YR}$ ), and the ratio of maximum safe extraction capacity reduction due to  
525 nanoplastic retention to maximum safe extraction capacity ( $RR_{SY}$ ) versus ( $a_1$ - $a_3$ )  
526 dispersivity, ( $b_1$ - $b_3$ ) hydraulic conductivity, and ( $c_1$ - $c_3$ ) recharge rate.

527 Fig. 8(a) and (b) present the theoretically derived maximum safe pumping rate  
528 near the freshwater lens center (Tang et al., 2021) and the actual maximum safe  
529 pumping rate, respectively. Under standard pumping conditions, the presence of a  
530 transition zone reduces the effective area of the freshwater lens by 16.12% and its  
531 thickness by 7.77 m. The position of pumping wells directly influences pumping rates:  
532 as the distance from the central region increases, pumping rates decrease linearly, as  
533 expressed in Equation (10). Simulation results demonstrate that the maximum safe  
534 pumping rate of freshwater lenses does not exhibit a perfect linear correlation with the  
535 distance from the surface central axis. During shallow pumping, higher rates may  
536 even be achieved near the coastal sides due to the low-velocity zone in the center. The  
537 actual maximum safe pumped volume occurs at  $x=10$  cm, corresponding to two-thirds  
538 of the island's width from the central axis, with a pumping rate of  $2.667 \times 10^{-5}$  kg/s  
539 (200% of the theoretical value). At the center, the rate decreases to  $2.480 \times 10^{-5}$  kg/s,  
540 equivalent to 62% of the theoretical value. Under idealized strip-shaped island  
541 hydrodynamic conditions, seawater infiltrates from both bottom sides, forming an  
542 outflow zone at the top of the coastline, with a "stagnation zone" emerging in the  
543 island center—a phenomenon confirmed in previous studies. Owing to the slow,  
544 predominantly vertical flow in the central region, residual brackish water persists and  
545 disperses upward primarily via vertical dispersion. Thus, for single-well pumping  
546 projects on small idealized strip-shaped islands, central pumping may not be optimal,  
547 whereas lateral single-well operations can yield higher freshwater outputs. For deep  
548 pumping, given that freshwater lenses on such islands are approximately semicircular,  
549 deeper pumping is feasible near the center.

550 Fig. 8(c) illustrates that nanoplastic concentration constraints reduce freshwater  
551 lens volume by 13-28%, with more significant reductions in areas farther from the



552 island's surface central axis, attributed to the uneven distribution of the nanoplastic  
553 transition zone. With respect to the reduction in maximum safe pumping rates, Fig.  
554 8(d) demonstrates the decline in pumped volumes at the island center when  
555 nanoplastic concentration limits are considered. Centered at the pumping point ( $x=20$   
556 cm,  $y=0$  cm), the maximum safe pumped volume gradually decreases with increasing  
557 distance from this center due to nanoplastic concentration restrictions. Near the  
558 seawater boundary, the transition zone completely covers the area within 10 cm of the  
559 shoreline. Under the 1%  $C_{nps}$  concentration limit, regions deeper than 25 mm are  
560 designated as non-exploitable zones. This phenomenon arises because the nanoplastic  
561 transition zone is relatively extended in the island's central region. Certain central  
562 regions exhibit pathway advantages, facilitating faster nanoplastic accumulation into  
563 wells. Near the seawater boundary, exploitable volumes decrease due to the influence  
564 of seawater nanoplastic source concentrations. Consequently, the combined effect of  
565 these two factors results in the highest exploitable volumes occurring in the upper  
566 regions near the central axis.



567

568 Fig. 8. Combined effects of pumping depth ( $d$ ) and shore distance ( $x_m$ ) on (a)  
 569 theoretical maximum safe extraction capacity ( $Q_{Tmax}$ ), (b) actual maximum safe  
 570 extraction capacity ( $Q_{Amax}$ ), (c) freshwater lens volume reduction rate ( $VR$ ), and (d)  
 571 the ratio of maximum safe extraction capacity reduction due to nanoplastic retention  
 572 to maximum safe extraction capacity ( $RRSY$ ).

#### 573 4. Conclusion

574 This study established a coupled variable-density groundwater flow and transport  
 575 model to explore nanoplastic migration in the freshwater lenses of idealized strip  
 576 islands under pumping scenarios. By integrating laboratory-calibrated parameters  
 577 with field-scale simulations, we identify fundamental differences between nanoplastic  
 578 and traditional solute transport processes and evaluate their implications for  
 579 groundwater management in island aquifers. Key conclusions are summarized as



580 follows:

581 (1) Nanoplastic transport differs fundamentally from dissolved salt transport. In  
582 contrast to dissolved salts, whose behavior is mainly regulated by advection and  
583 dispersion, nanoplastics are further affected by particle-specific processes, such as  
584 adsorption-desorption, clogging, and filtration. The higher effective dispersivity leads  
585 to earlier breakthrough at extraction wells and the development of broader  
586 contaminant transition zones compared to salinity alone.

587 (2) Transport behavior exhibits strong scale dependence. Laboratory-scale  
588 simulations showed rapid contamination and prominent "upper cone" formation  
589 within minutes, whereas field-scale simulations demonstrated attenuated upward  
590 coning and much longer stabilization times on the order of years. This contrast  
591 highlights the importance of multi-scale modeling when extrapolating experimental  
592 results to real-world island aquifers.

593 (3) Dispersivity is the dominant control on nanoplastic risk. Among the  
594 evaluated parameters, nanoplastic dispersivity exerts the strongest influence on  
595 contaminant accumulation in extraction wells, with hydraulic conductivity and  
596 recharge rates playing secondary but important roles. When nanoplastic dispersivity  
597 exceeds approximately 17 times that of dissolved solutes, the contaminant plume can  
598 fully envelop the well screen, reducing the maximum safe extraction rate by 37-50%  
599 compared to salinity-based thresholds.

600 (4) Well placement strategies must account for nanoplastic transition zones.  
601 Traditional guidelines based solely on salinity intrusion may not minimize  
602 contamination risks. Simulations suggest that central pumping locations are not  
603 always optimal; lateral well placement (approximately two-thirds of the distance from  
604 the island centerline) can increase freshwater yield while reducing nanoplastic  
605 contamination potential.

606 Several simplifying assumptions were adopted in this study, including  
607 homogeneous aquifer properties, idealized boundary conditions, and limited



608 representation of nanoplastic diversity. In practice, aquifer heterogeneity, tidal  
609 fluctuations, storm events, and the wide range of environmental nanoplastic properties,  
610 including particle size distribution, aging state, and surface chemistry, may further  
611 influence transport behavior. Moreover, only two synthetic nanoplastic types of  
612 synthetic nanoplastics were considered here, whereas natural systems contain a  
613 broader and more complex spectrum of particles. Despite these limitations, the  
614 present study establishes a mechanistic framework for evaluating nanoplastic  
615 transport in coastal freshwater lenses. By coupling variable-density flow with  
616 particle-specific transport processes and quantifying impacts on safe extraction  
617 thresholds, this study provides a process-based basis for revising groundwater  
618 management strategies in island settings. Future research should incorporate  
619 heterogeneous aquifer structures, dynamic hydrological forcing, and broader  
620 nanoplastic characteristics to enhance predictive capability and support water security  
621 in increasingly plastic-polluted coastal environments.

#### 622 **Data availability**

623 The data of this study can be found in Zheng (2026,  
624 <https://zenodo.org/records/19150343> ).

#### 625 **Author contributions**

626 TYZ: Conceptualization, Writing-Original Draft, Methodology, Resources,  
627 Writing-Review and Editing, Funding acquisition, Supervision.

628 CXM: Investigation, Software, Writing-Original Draft, Writing-Review and Editing,  
629 Visualization, Data Curation, Conceptualization.

630 SBG: Methodology, Formal Analysis, Investigation, Visualization, Writing-Review  
631 and Editing.



632 JL: Writing-Review and Editing, Methodology, Supervision, Conceptualization.

633 **Competing interests**

634 The contact author has declared that none of the authors has any competing interests.

635 **Financial support**

636 This work was supported by the National Natural Science Foundation of China (No.

637 42422207), Taishan Scholars Program of Shandong Province (No. tsqn202408078)

638 and the Postdoctoral Fellowship Program of CPSF under Grant Number

639 GZC20250290.

640



## 641 Reference

- 642 Abdoulhalik, A., & Ahmed, A. A. (2018), Transient investigation of saltwater upconing in  
643 laboratory-scale coastal aquifer, *Estuarine, Coastal and Shelf Science*, 214, 149-160.  
644 <https://doi.org/10.1016/j.ecss.2018.09.024>.
- 645 Al Harraq, A., & Bharti, B. (2022), Microplastics through the Lens of Colloid Science, *ACS*  
646 *Environmental Au*, 2(1), 3-10. <https://doi.org/10.1021/acsenvironau.1c00016>.
- 647 Alsumaiei, A. A., & Bailey, R. T. (2018), Quantifying threats to groundwater resources in the  
648 Republic of Maldives Part I: Future rainfall patterns and sea-level rise, *Hydrological*  
649 *Processes*, 32(9), 1137-1153. <https://doi.org/10.1002/hyp.11480>.
- 650 Amirmoshiri, M., Zhang, L., Puerto, M. C., Tewari, R. D., Bahrim, R. Z. B. K., Farajzadeh, R.,  
651 Hirasaki, G. J., & Biswal, S. L. (2020), Role of Wettability on the Adsorption of an Anionic  
652 Surfactant on Sandstone Cores, *Langmuir*, 36(36), 10725-10738.  
653 <https://doi.org/10.1021/acs.langmuir.0c01521>.
- 654 Babakhani, P., Bridge, J., Doong, R. A., & Phenrat, T. (2017), Continuum-based models and  
655 concepts for the transport of nanoparticles in saturated porous media: A state-of-the-science  
656 review, *Advances in colloid and interface science*, 246, 75-104.  
657 <https://doi.org/10.1016/j.cis.2017.06.002>.
- 658 Babu, R., Park, N., & Nam, B. (2020), Regional and well-scale indicators for assessing the  
659 sustainability of small island fresh groundwater lenses under future climate conditions,  
660 *Environmental Earth Sciences*, 79(1), 47. <https://doi.org/10.1007/s12665-019-8773-3>.
- 661 Bailey, R. T., & Jenson, J. W. (2014), Effects of Marine Overwash for Atoll Aquifers:  
662 Environmental and Human Factors, *Groundwater*, 52(5), 694-704.  
663 <https://doi.org/10.1111/gwat.12117>.
- 664 Chen, G., Zou, Y., Xiong, G., Wang, Y., Zhao, W., Xu, X., Zhu, X., Wu, J., Song, F., & Yu, H.  
665 (2024), Microplastic transport and ecological risk in coastal intruded aquifers based on a  
666 coupled seawater intrusion and microplastic risk assessment model, *Journal of hazardous*  
667 *materials*, 135996. <https://doi.org/10.1016/j.jhazmat.2024.135996>.
- 668 Chen, Q., Zhang, L., Shen, C., & Lu, C.(2024), Effects of groundwater pumping on pore water  
669 flow and salt transport in tide-controlled unconfined coastal aquifers, *Hydrological Processes*,  
670 38(8), e15261. <https://doi.org/10.1002/hyp.15261>.
- 671 Coulon, C., Lemieux, J. M., Pryet, A., Bayer, P., Young, N. L., & Molson, J. (2022), Pumping  
672 Optimization Under Uncertainty in an Island Freshwater Lens Using a Sharp-Interface  
673 Seawater Intrusion Model, *Water Resources Research*, 58(8).  
674 <https://doi.org/10.1029/2021WR031793>.
- 675 Cui, X., Zhu, C., Hu, M., Wang, R., & Liu, H. (2021), Permeability of porous media in coral reefs,  
676 *Bulletin of Engineering Geology and the Environment*, 80(6), 5111-5126.  
677 <https://doi.org/10.1007/s10064-020-02082-5>.
- 678 Dagan, G., & Bear, J. (1968), Solving The Problem Of Local Interface Upconing In A Coastal  
679 Aquifer By The Method Of Small Perturbations, *Journal of Hydraulic Research*, 6(1), 15-44.  
680 <https://doi.org/10.1080/00221686809500218>.
- 681 Dose, E. J., Stoeckl, L., Houben, G. J., Vacher, H. L., Vassolo, S., Dietrich, J., & Himmelsbach, T.  
682 J. J. o. H.(2014), Experiments and Modeling of Freshwater Lenses in Layered Aquifers:  
683 Steady State Interface Geometry, 509, 621-630.



- 684 <http://dx.doi.org/10.1016/j.jhydrol.2013.10.010>.
- 685 Gao, C., Zheng, T., Chang, Q., Zheng, X., Song, X., & Luo, J. (2025), Dynamics of Irregular  
686 Freshwater Lenses Evolution in Thin Aquifers of Reclaimed Circular Islands, *Water*  
687 *Resources Research*, 61(7), e2024WR038880. <https://doi.org/10.1029/2024WR038880>.
- 688 Gelhar, L. W., Welty, C., & Rehfeldt, K. R. (1992), A critical review of data on field-scale  
689 dispersion in aquifers, *Water Resources Research*, 28(7), 1955-1974.  
690 <https://doi.org/10.1029/92WR00607>.
- 691 Houben, G., & Post, V. E. A. (2017), The first field-based descriptions of pumping-induced  
692 saltwater intrusion and upconing, *Hydrogeology Journal*, 25(1), 243-247.  
693 <https://doi.org/10.1007/s10040-016-1476-x>.
- 694 Isobe, A., Iwasaki, S., Uchida, K., & Tokai, T. (2019), Abundance of non-conservative  
695 microplastics in the upper ocean from 1957 to 2066, *Nature Communications*, 10(1), 417.  
696 <https://doi.org/10.1038/s41467-019-08316-9>.
- 697 Johnson, W. P. (2020), Quantitative Linking of Nanoscale Interactions to Continuum-Scale  
698 Nanoparticle and Microplastic Transport in Environmental Granular Media, *Environmental*  
699 *Science & Technology*, 54(13), 8032-8042. <https://doi.org/10.1021/acs.est.0c01172>.
- 700 Ketabchi, H., Mahmoodzadeh, D., Ataie-Ashtiani, B., Werner, A. D., & Simmons, C. T. (2014),  
701 Sea-level rise impact on fresh groundwater lenses in two-layer small islands, *Hydrological*  
702 *Processes*, 28(24), 5938-5953. <https://doi.org/10.1002/hyp.10059>.
- 703 Koelmans, A. A., Redondo-Hasselerharm, P. E., Nor, N. H. M., de Ruijter, V. N., Mintenig, S. M.,  
704 & Kooi, M. (2022), Risk assessment of microplastic particles, *Nature Reviews Materials*,  
705 7(2), 138-152. <https://doi.org/10.1038/s41578-021-00411-y>.
- 706 Koutnik, V. S., Leonard, J., Alkidim, S., DePrima, F. J., Ravi, S., Hoek, E. M. V., & Mohanty, S. K.  
707 (2021), Distribution of microplastics in soil and freshwater environments: Global analysis  
708 and framework for transport modeling, *Environmental pollution (Barking, Essex : 1987)*, 274,  
709 116552. <https://doi.org/10.1016/j.envpol.2021.116552>.
- 710 Li, J., Liu, H., & Paul Chen, J. (2018), Microplastics in freshwater systems: A review on  
711 occurrence, environmental effects, and methods for microplastics detection, *Water Research*,  
712 137, 362-374. <https://doi.org/10.1016/j.watres.2017.12.056>.
- 713 Li, M., Zhang, M., Rong, H., Zhang, X., He, L., Han, P., & Tong, M. (2021), Transport and  
714 deposition of plastic particles in porous media during seawater intrusion and  
715 groundwater-seawater displacement processes, *Science of The Total Environment*, 781,  
716 146752. <https://doi.org/10.1016/j.scitotenv.2021.146752>.
- 717 Liu, Y., Zheng, T., Guo, B., Jiang, S., Cao, M., & Zheng X. (2024), Adsorption Characteristics of  
718 Dissolved Organic Nitrogen on Aquifer Porous Media: The Role of Media Particle Size, *ACS*  
719 *ES&T Water*, 4(5), 2170-2180. <https://doi.org/10.1021/acsestwater.3c00815>.
- 720 Moore, C. J., Moore, S. L., Leecaster, M. K., & Weisberg, S. B. (2001), A Comparison of Plastic  
721 and Plankton in the North Pacific Central Gyre, *Marine Pollution Bulletin*, 42(12),  
722 1297-1300. [https://doi.org/10.1016/S0025-326X\(01\)00114-X](https://doi.org/10.1016/S0025-326X(01)00114-X).
- 723 Muskat, M. (1937), The Flow of Fluids Through Porous Media, *Journal of Applied Physics*, 8(4),  
724 274-282. <https://doi.org/10.1063/1.1710292>.
- 725 Ranjan, V. P., Joseph, A., Sharma, H. B., & Goel, S. (2023), Preliminary investigation on effects of  
726 size, polymer type, and surface behaviour on the vertical mobility of microplastics in a  
727 porous media, *Science of The Total Environment*, 864, 161148.



- 728 <https://doi.org/10.1016/j.scitotenv.2022.161148>.
- 729 Reddy, M. S., Shaik, B., Adimurthy, S., & Ramachandraiah, G. (2006), Description of the small  
730 plastics fragments in marine sediments along the Alang-Sosiya ship-breaking yard, India,  
731 Estuarine, Coastal and Shelf Science, 68(3), 656-660.  
732 <https://doi.org/10.1016/j.ecss.2006.03.018>.
- 733 Ren, Z., Gui, X., Xu, X., Zhao, L., Qiu, H., & Cao, X. (2021), Microplastics in the  
734 soil-groundwater environment: Aging, migration, and co-transport of contaminants - A  
735 critical review, Journal of hazardous materials, 419, 126455.  
736 <https://doi.org/10.1016/j.jhazmat.2021.126455>.
- 737 Ren, Z., Gui, X., Xu, X., Zhao, L., Qiu, H., Wang, X., & Cao, X. (2022), Weathering of  
738 microplastics and their enhancement on the retention of cadmium in coastal soil saturated  
739 with seawater, Journal of hazardous materials, 440, 129850.  
740 <https://doi.org/10.1016/j.jhazmat.2022.129850>.
- 741 Sayre, R., Noble, S., Hamann, S., Smith, R., Wright, D., Breyer, S., Butler, K., Van Graafeiland,  
742 K., Frye, C., Karagulle, D., Hopkins, D., Stephens, D., Kelly, K., Basher, Z., Burton, D.,  
743 Cress, J., Atkins, K., Van Sistine, D. P., Friesen, B., Allee, R., Allen, T., Aniello, P., Asaad, I.,  
744 Costello, M. J., Goodin, K., Harris, P., Kavanaugh, M., Lillis, H., Manca, E., Muller-Karger,  
745 F., Nyberg, B., Parsons, R., Saarinen, J., Steiner, J., & Reed, A (2019), A new 30 meter  
746 resolution global shoreline vector and associated global islands database for the development  
747 of standardized ecological coastal units, Journal of Operational Oceanography, 12(sup2),  
748 S47-S56. <https://doi.org/10.1080/1755876X.2018.1529714>.
- 749 Sharan, A., Lal, A., & Datta, B. (2021), A review of groundwater sustainability crisis in the Pacific  
750 Island countries: Challenges and solutions, Journal of Hydrology, 603, 127165.  
751 <https://doi.org/10.1016/j.jhydrol.2021.127165>.
- 752 Singh, A., Chauhan, A., & Gaur, R. (2025), A comprehensive review on the synthesis, properties,  
753 environmental impacts, and chemiluminescence applications of polystyrene (PS), Discover  
754 Chemistry, 2(1), 47. <https://doi.org/10.1007/s44371-025-00125-y>.
- 755 Stoeckl, L., & Houben, G. (2012), Flow dynamics and age stratification of freshwater lenses:  
756 Experiments and modeling, Journal of Hydrology, 458-459, 9-15.  
757 <https://doi.org/10.1016/j.jhydrol.2012.05.070>.
- 758 Sussarellu, R., Suquet, M., Thomas, Y., Lambert, C., Fabioux, C., Pernet, M. E. J., Le Goïc, N.,  
759 Quillien, V., Mingant, C., Epelboin, Y., Corporeau, C., Guyomarch, J., Robbens, J., Paul-Pont,  
760 I., Soudant, & P., Huvet, A. (2016), Oyster reproduction is affected by exposure to  
761 polystyrene microplastics, Proceedings of the National Academy of Sciences, 113(9),  
762 2430-2435. <https://doi.org/10.1073/pnas.1519019113>.
- 763 Tang, Y., Lu, C., & Luo, J. (2022), An Analytical solution for groundwater lens pumping in a  
764 three-dimensional rectangular island, Journal of Hydrology, 617, 128928.  
765 <https://doi.org/10.1016/j.jhydrol.2022.128928>.
- 766 Tang, Y., Lu, C., & Luo J. (2024), Optimizing groundwater pumping in small island groundwater  
767 lenses: An analytical approach, Journal of Hydrology, 629, 130579.  
768 <https://doi.org/10.1016/j.jhydrol.2023.130579>.
- 769 Tang, Y., Rathore, S., Lu, C., & Luo, J. (2020), Development of Groundwater Lens for Transient  
770 Recharge in Strip Islands, Journal of Hydrology, 590, 125209.  
771 <https://doi.org/10.1016/j.jhydrol.2020.125209>.



- 772 Tang, Y., Yan, M., Wang, X., Lu, C., & Luo, J. (2021), Experimental and modeling investigation  
773 of pumping from a fresh groundwater lens in an idealized strip island, *Journal of Hydrology*,  
774 602, 126734. <https://doi.org/10.1016/j.jhydrol.2021.126734>.
- 775 ten Hietbrink, S., Materić, D., Holzinger, R., Groeskamp, S., & Niemann, H. (2025), Nanoplastic  
776 concentrations across the North Atlantic, *Nature*, 643(8071), 412-416.  
777 <https://doi.org/10.1038/s41586-025-09218-1>.
- 778 Thompson, R. C., Courtene-Jones, W., Boucher, J., Pahl, S., Raubenheimer, K., & Koelmans, A. A.  
779 (2024), Twenty years of microplastic pollution research—what have we learned?, *Science*,  
780 386(6720), eadl2746. <https://doi.org/10.1126/science.adl2746>.
- 781 van Genuchten, M.T. (1980), A Closed-form Equation for Predicting the Hydraulic Conductivity  
782 of Unsaturated Soils. *Soil Science Society of America Journal*, 44: 892-898.  
783 <https://doi.org/10.2136/sssaj1980.03615995004400050002x>.
- 784 Voss, C., & Provost, A. M. (2002), SUTRA: A model for 2D or 3D saturated-unsaturated,  
785 variable-density ground-water flow with solute or energy transport, Report Rep. 2002-4231.  
786 <https://doi.org/10.3133/wri024231>.
- 787 Waldschläger, K., & Schüttrumpf, H. (2020), Infiltration Behavior of Microplastic Particles with  
788 Different Densities, Sizes, and Shapes—From Glass Spheres to Natural Sediments,  
789 *Environmental Science & Technology*, 54(15), 9366-9373.  
790 <https://doi.org/10.1021/acs.est.0c01722>.
- 791 Wang, R., Shu, L., Zhang, R., & Ling, Z. (2023), Determination of Exploitable Coefficient of  
792 Coral Island Freshwater Lens Considering the Integrated Effects of Lens Growth and  
793 Contraction, *Water*, 15(5), 890, doi: 10.3390/w15050890.  
794 <https://doi.org/10.3390/w15050890>.
- 795 Wang, X., Bolan, N., Tsang, D. C. W., Sarkar, B., Bradney, L., & Li, Y. (2021), A review of  
796 microplastics aggregation in aquatic environment: Influence factors, analytical methods, and  
797 environmental implications, *Journal of hazardous materials*, 402, 123496.  
798 <https://doi.org/10.1016/j.jhazmat.2020.123496>.
- 799 Wang, Z., & Sedighi, M. (2023), Dispersion properties of nanoplastic spheres in granular media at  
800 low Reynolds numbers, *Journal of Contaminant Hydrology*, 259, 104244.  
801 <https://doi.org/10.1016/j.jconhyd.2023.104244>.
- 802 Werner, A. D., Jakovovic, D., & Simmons, C. T. (2009), Experimental observations of saltwater  
803 up-coning, *Journal of Hydrology*, 373(1), 230-241.  
804 <https://doi.org/10.1016/j.jhydrol.2009.05.004>.
- 805 White, I., & Falkland, T. (2010), Management of freshwater lenses on small Pacific islands,  
806 *Hydrogeology Journal*, 18(1), 227-246. <https://doi.org/10.1007/s10040-009-0525-0>.
- 807 Yan, M., Lu, C., Werner, A. D., & Luo, J. (2021), Analytical, Experimental, and Numerical  
808 Investigation of Partially Penetrating Barriers for Expanding Island Freshwater Lenses, *Water  
809 Resources Research*, 57(3), e2020WR028386. <https://doi.org/10.1029/2020WR028386>.
- 810 Yang, J., Wang, Q., Heidbüchel, I., Xu, T., & Lu, C. (2025), Cut-off walls alter nitrogen loads and  
811 fluxes in small islands, *Journal of Hydrology*, 647, 132266.  
812 <https://doi.org/10.1016/j.jhydrol.2024.132266>.
- 813 Yao, Y., Andrews, C., Zheng, Y., He, X., Babovic, V., & Zheng, C. (2019), Development of Fresh  
814 Groundwater Lens in Coastal Reclaimed Islands, *Journal of Hydrology*, 573, 365-375.  
815 <https://doi.org/10.1016/j.jhydrol.2019.03.062>.



- 816 Yuan, C., Hu, L., Ren, Z., Xu, X., Gui, X., Gong, X., Wu, R., Sima, J., & Cao, X. (2024), Marine  
817 Microplastics Enhance Release of Arsenic in Coastal Aquifer during Seawater Intrusion  
818 Process, Journal of Hazardous Materials, 475, 134804.  
819 <https://doi.org/10.1016/j.jhazmat.2024.134804>.
- 820 Zheng, T. (2014), Numerical Analysis of Modeling Concepts for Salt Precipitation and Porosity -  
821 Permeability Evolution during Brine Evaporation.
- 822 Zheng, T., Meng, Y., Meng, X., Gao, S., Zhang, L., Zhang, B., Liu, T., & Luo, J. (2025), Influence  
823 of time-space variability of rainfall infiltration recharge on fresh groundwater lens, Physics of  
824 Fluids, 37(3), 036623. <https://doi.org/10.1063/5.0253940>.
- 825